Journal of MATERIALS RESEARCH

Article
DOI:10.1557/s43578-024-01479-2

Strain-and temperature-induced dilatancy in ZrNi thin film metallic glasses with nanoscale structural heterogeneities

R. Daudin[1,2,a], H. Idrissi[2,3], M. Coulombier[2], P. Lhuissier[1], A. Béché[2,3], J. Verbeeck[3], D. Schryvers[3], M. Ghidelli[4], J. P. Raskin[5], J-J. Blandin[1], T. U. Schülli[6], T. Pardoen[2,7]

[1] University Grenoble Alpes, CNRS, Grenoble INP, SIMaP, 38000 Grenoble, France
[2] IMMC, Université catholique de Louvain, B-1348 Louvain-La-Neuve, Belgium
[3] Electron Microscopy for Materials Science (EMAT), University of Antwerp, 2020 Antwerp, Belgium
[4] Laboratoire Des Sciences Des Procédés Et Des Matériaux (LSPM), CNRS, Université Sorbonne Paris Nord, 93430 Villetaneuse, France
[5] ICTEAM, Université catholique de Louvain, B-1348 Louvain-La-Neuve, Belgium
[6] The European Synchrotron ESRF, BP 220, 38043 Grenoble Cedex 9, France
[7] WEL Research Institute, Avenue Pasteur 6, 1300 Wavre, Belgium
[a] Address all correspondence to this author. e-mail: remi.daudin@simap.grenoble-inp.fr

Received: 7 March 2024; accepted: 29 October 2024

Thin film metallic glasses (TFMG) provide rich information on plastic phenomena owing to a more ductile behaviour than bulk counterparts. However, correlation between the macroscopic and the atomic strain for sub-micron scale specimens remains a challenge which is essential towards unravelling the origin of the mechanical properties. Here, complementary results were obtained combining high-resolution X-ray synchrotron scattering and in situ annealing transmission electron microscopy measurements on ZrNi thin freestanding films showing remarkable strength/ductility balance. The evolution of the structure factor shows the occurrence of spatially homogeneous and isotropic atomic dilatancy without shear banding upon tensile loading at room temperature. The in situ TEM results reveal that such dilatancy is also triggered during thermal annealing but only in undeformed samples. The discussion aims at linking this behaviour to the specific microstructure of the films, which involves nanoscale chemical/density heterogeneities inherited from the deposition process, and to the mechanical properties.

Introduction

Metallic glasses (MG) are reputed for their exceptional tensile strength involving large elastic strain. However, they suffer from a limited capacity to develop homogeneous plasticity at room temperature, especially in tension. Brittleness essentially stems from premature strain localization events leading to the propagation of catastrophic shear bands and to the subsequent failure. Hence, a major lever to enhance the capacity of MG to produce more homogeneous plastic flow lies in the mitigation of the shear banding nucleation and/or propagation process [1–3] to suppress or at least delay fracture.

The early work of Volkert et al. reported the absence of catastrophic shear banding during plastic deformation when compressing pillars with diameters below 500 nm [4]. This study was at the origin of a relatively recent research focus on the mechanical response of MG at small dimensions that differ from the bulk counterparts [5–7]. This is intriguing because the absence of grains in MG, and therefore of grain boundaries, should imply mechanical properties independent of the specimen size. However, differences are observed on the elastic response [8], on the yield stress [9–11], on the elastic-to-plastic transition [9, 12], on the plastic deformation mechanisms (*i.e.* shear banding) [11, 13] and on the fracture behaviour [11, 14, 15], with non-obvious correlations between the different regimes.

Still, the "size-effect" term remains an equivocal shortcut to encompass various underlying physical features influencing the transition between shear-band dominated to homogeneous plastic yielding. Therefore, caution must be advised when attributing unexpected mechanical behaviour to a scale effect *only* when it can be connected to a switch in the underlying mechanisms when down-sizing, either intrinsically or extrinsically [5, 6, 16]. Indeed, in addition to energetic

considerations showing the existence of a critical dimension below which mature shear bands cannot nucleate or propagate [4, 9, 11], surface stresses [17], e-beam irradiation [18], strain rates [10, 18], surface roughness [19], surface-to-volume ratio [20] and/or a lack of structural defects [9, 13] are also reported to influence the mechanical response at small scales. In parallel, other studies claim for the size-independency of the mechanical properties [21] or for a size dependency subordinated by the cohesion of the atomic bonds [22]. A clear element of complexity in the quest to separate and quantify these possible effects is the extreme difficulty to characterise experimentally MG at small scales. This is a challenge both in terms of sample processing, mechanical testing and structural characterization. More specifically, there is a major need for (i) producing pristine metallic glasses with small dimensions and (ii) correlating the macroscopic mechanical response to the affine and non-affine atomic structural changes activated inside the material upon loading.

In a previous study, Ghidelli et al. reported that decreasing the thickness of $Zr_{65}Ni_{35}$ TFMG leads to larger yield stresses as well as to homogeneous and large plastic deformation when tested in tension using an on-chip platform [9]. More recently, using advanced high-resolution transmission electron microscopy (HR-TEM), Idrissi et al. demonstrated that, beyond sample dimensions, the intricate structure at the atomic cluster length scale also plays a key role [23]. Indeed, $Zr_{65}Ni_{35}$ (At.%) TFMG were found to display atomic density and chemical heterogeneities of 2–3 nm in size as well as continuous disruption of the local atomic order with increasing plastic deformation. This heterogeneous atomic organization associated to a local variation of excess energy is at the origin of the mediation of the local shear providing a stress delocalization principle, hence confirming that structural heterogeneities also have a pivotal role in the structure–property relationship in MG [24–26]. Bridging the macroscopic [9] and the atomic cluster [23] scales is an important step towards understanding the structural changes arising during the deformation of TFMG. To address this challenge, Gammer et al. developed strain mapping in metallic glasses in TEM using precession nanodiffraction [27, 28]. However, this technique is not suitable for the characterization of wide areas and samples with thickness larger than few nanometers. Concerning X-rays, the early work of Poulsen et al. revealed that the use of X-ray scattering on metallic glasses is a powerful tool to measure atomic strain [29]. Generally, high energy X-rays are used to probe relatively thick bulk metallic glasses (BMG) [30] and to expand the accessible reciprocal space range [31], but at the expense of spot size and/or flux. For instance, Scudino et al. successfully analysed the atomic strain distribution inside BMG in the near crack tip region [32], across shear bands [33] and around structural heterogeneities [34], but with a limited spatial resolution preventing the study of very small specimens, such as thin films.

In order to further investigate experimentally the link between atomistic strain and macroscopic deformation, we combine, as shown in Fig. 1, three cutting-edge techniques to jointly study both the macroscopic response and local atomic mechanisms: (i) "on-chip" tensile tests with specimens processed by physical vapour deposition providing consistent and reproducible mechanical data [35, 36], (ii) highly focussed synchrotron X-ray beam [37] for the acquisition of the spatial distribution of the local atomic strain and (iii) advanced in situ heating HR-TEM experiments revealing the evolution of the atomic structure with temperature [23] (see the Materials and Methods section). We show that both strain- and temperature-induced homogeneous atomic dilatancy can develop in the pristine microstructure of 360-nm-thick $Zr_{42}Ni_{58}$ and $Zr_{65}Ni_{35}$TFMG suggesting complex atomic rearrangement arising from the pristine as-deposited microstructure. The detailed discussion aims at answering the following scientific questions: how does the spatial distribution of the atomic strain evolve inside TFMG deformed in tension at RT? How does it correlate to the macroscopic strain and to the mechanical properties? Does the pristine deposited atomic structure play a role?

Results

X-ray diffraction

Figure 1(b) shows the stress–strain response of the $Zr_{42}Ni_{58}$ 360-nm-thick film. In a previous study, Ghidelli et al. revealed that increasing the Ni content decreases the atomic density due to the larger amount of Zr–Ni bonds and to an increase of stronger atomic bonds [38]. Therefore, compared to the $Zr_{65}Ni_{35}$ composition published elsewhere [9], the $Zr_{42}Ni_{58}$ TFMG is expected to be less ductile. This is indeed the case as the $Zr_{42}Ni_{58}$ composition shows an ultimate strain of 7%, whereas it is almost equal to 10% for a $Zr_{65}Ni_{35}$ specimen of same thickness and geometry (width: 2 µm, length: 50 µm, see Fig S1). The last unbroken specimen in the present series is the 33rd (noted S33) for the $Zr_{42}Ni_{58}$ films and the 40th (noted S40) for the $Zr_{65}Ni_{35}$ composition. A 7% total elongation is still a high value for a metallic glass involving significant plastic deformation. For the $Zr_{42}Ni_{58}$ films, the ultimate stress is equal to 2200 MPa. This value is comparable to the ones found for the $Zr_{65}Ni_{35}$ compositions (Fig S1 and [9]) but were expected to be higher compared to previous studies [38, 39]. The structural investigation under mechanical loading of these two compositions offers the possibility to investigate the impact of the Zr/Ni ratio as well as the relationship between the atomic and the macroscopic strain up to failure.

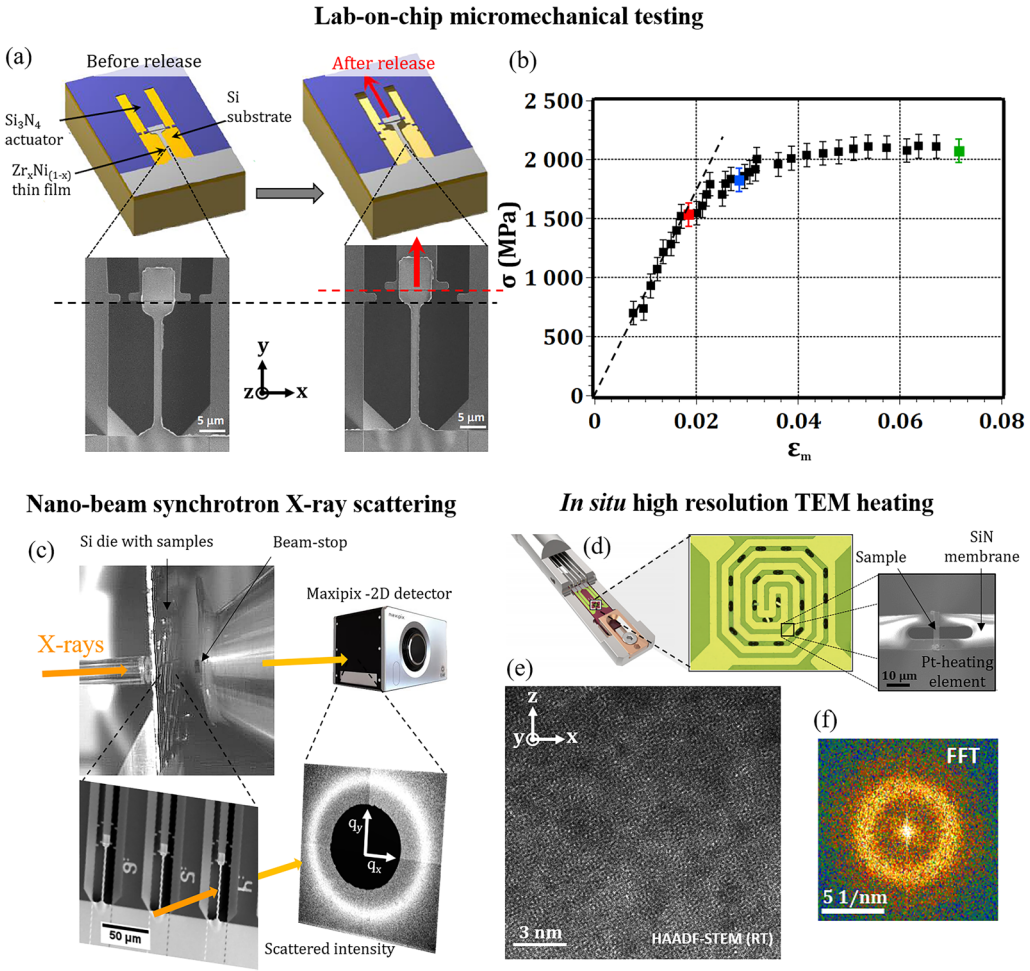

Figure 1: (a) SEM images of an unreleased and a released specimen illustrating the extraction of the macroscopic strain together with (b) the strain–stress response of the $Zr_{42}Ni_{58}$ (at%) 360-nm-thick film. The highlighted dots correspond to the specimen 9, 17 and 33 of the series probed by X-ray scattering (see main text). (c) Illustration of the ESRF ID01 set-up to probe the samples in transmission. (d) Wildfire heating stage from DENS solutions. Cross-sectional foil is fixed and thinned on the heating chip by FIB. (e) High-resolution HAADF-STEM micrograph and (f) its FFT on as-deposited $Zr_{65}Ni_{35}$ (at%) TFMGs.

Figure 2(a) superimposes the averaged elliptical fit of the scattered intensities measured at each location within the three $Zr_{42}Ni_{58}$ increasingly deformed specimens [S9, S17 and S33, see Fig. 1(b)]. For the $Zr_{42}Ni_{58}$ films, the signal from the unloaded state was acquired on free beams (Fig S1). The perfect ring shape of the scattering signal (Fig S3(a)) confirms the lack of anisotropy in the reference state and a higher atomic density compared to the $Zr_{65}Ni_{35}$ composition due to a higher amount of Ni–Ni bonds [39]. When zooming at the top of the ellipses, *i.e.* along the loading direction q_y in reciprocal space, the averaged maximum of intensity shifts closer to the origin of the reciprocal space with increasing macroscopic deformation. This indicates that, as expected, the mean interatomic distances increase along the loading direction, *i.e.* atomic bonds are stretched. Along the transverse direction q_x, a shift of the maximum of intensity towards higher values with increasing macroscopic strain is usually observed in bulk metallic glasses [30, 40] due to Poisson transverse contraction, which is observed here if the scattered intensities between the S9, S17 and S33 specimens are compared [Fig. 2(a) and Fig S4]. However, the contraction is not observed when comparing to the unloaded state: the S9, S17 and S33 average intensity maxima are all positioned at lower q_x values compared to the unloaded state. Therefore, the three deformed states exhibit larger averaged interatomic distances with respect to the unloaded state along the transverse direction q_x [see Fig. 2]. This evolution of the scattering signal was unexpected. This finding means that the $Zr_{42}Ni_{58}$ thin films undergo atomic expansion in the transverse direction upon tension at small to moderate stretching levels (< 2%) still within a globally elastic regime. This indicates that the pristine microstructure of the glass contains features that are susceptible to undergo such atomic reorganisation.

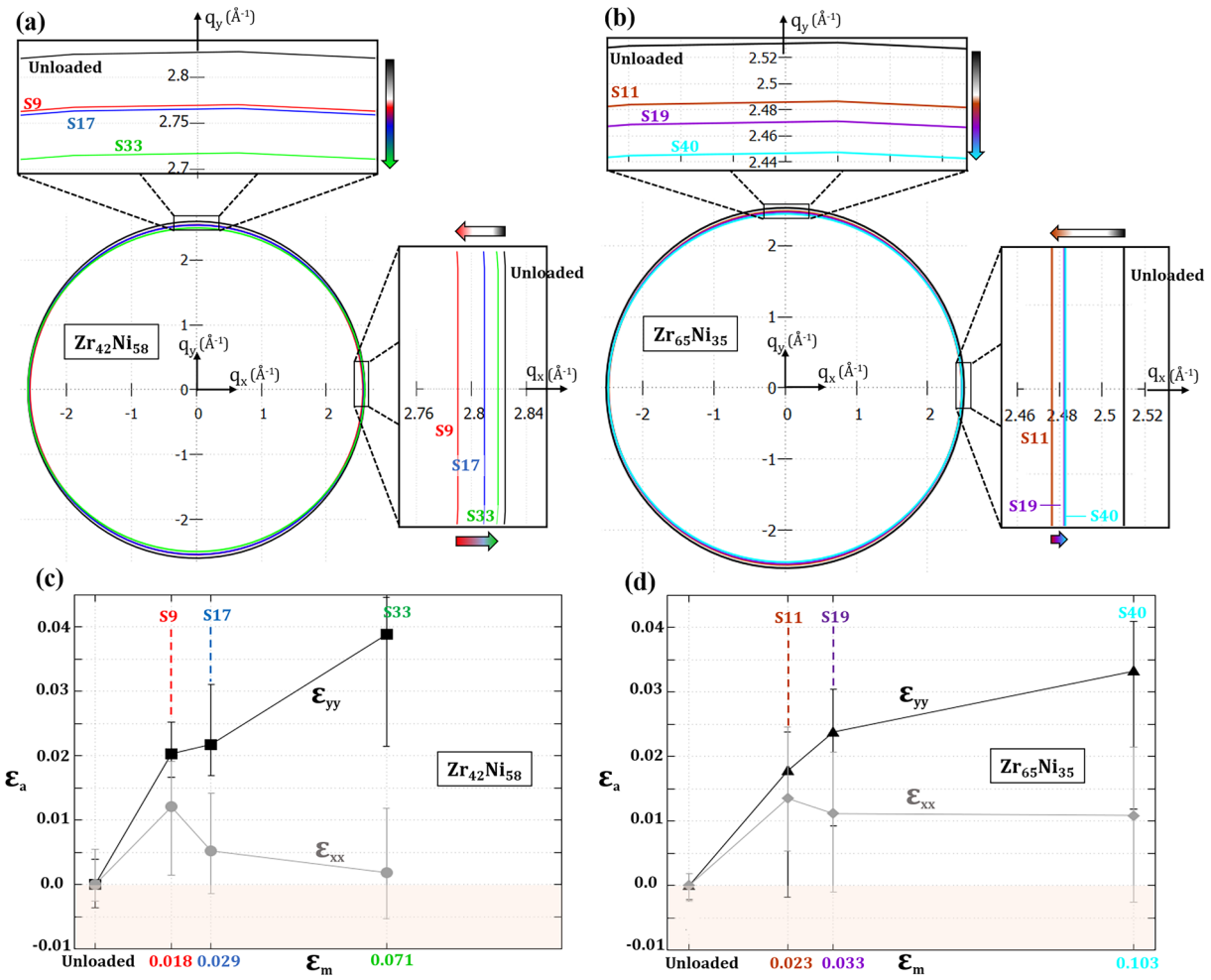

Figure 2: Averaged elliptic fit* of the scattered intensity recorded in (a) the unloaded state (black), S9 (red), S17 (blue) and S33 (green) specimen for $Zr_{42}Ni_{58}$ and in (b) the unloaded state (black), S11 (brown), S19 (violet) and S40 (cyan) specimen for $Zr_{65}Ni_{35}$. Evolution of the average atomic strains ε_{yy} (along the loading direction *y*) and ε_{xx} (along the transverse direction *x*) as a function of the macroscopic strain ε_m for (c) the $Zr_{42}Ni_{58}$ and (d) the $Zr_{65}Ni_{35}$ compositions. The vertical bars indicate the two extrema measured in each sample. *The ellipses were plotted using the average parameters computed from the 2D elliptical fit of all the 2D images recorded in each specimen.

A similar behaviour is observed for the $Zr_{65}Ni_{35}$ composition. In this case, the reference state (unloaded) was taken far from the deformed area, at the bottom of specimen 40 (Fig S1), so that a slight anisotropy of the scattered intensity differing along *y* and *x* in the unloaded state are recorded (Fig S3(b)). This slight degree of anisotropy of the reference state for the $Zr_{65}Ni_{35}$ films can potentially induce more scattered atomic strain values (ε_a) but the trend confirms the observation made for the $Zr_{42}Ni_{58}$ composition: the mean elliptical scattered intensities from the three deformed specimens (S11, S19 and S40) remain inside the scattering signal of the unloaded specimen indicating that the bond spacing is increasing along both q_y and q_x for this composition [see Fig. 2]. Again, this behaviour is observed in the small deformation regime. The increase of the atomic bond lengths both in the longitudinal and transverse directions for both compositions is further highlighted in Fig. 2(c) and (d) showing the evolution of the atomic strains ε_a with the macroscopic strain ε_m along q_y (ε_{yy}) and q_x (ε_{xx}). For the two compositions, ε_{yy} steadily increases with increasing macroscopic deformation in order to accommodate the imposed displacement, while ε_{xx} increases at first and then decreases. Note that the average values of ε_{xx} remain positive even for the last unbroken specimens ($Zr_{42}Ni_{58}$-S33 and $Zr_{65}Ni_{35}$-S40). It is remarkable that this behaviour is also captured macroscopically (Figure S4) even if accurate measurements of the specimen's width by SEM can be difficult and that a discrepancy between $\varepsilon_{a(x)}$ and $\varepsilon_{m(x)}$ is not yet fully elucidated.

The X-ray data of Fig. 2 reveal several key features: (i) the atomic strain inside these TFMG can reach very high values (up to about 0.04 in the specimen $Zr_{42}Ni_{58}$-S33), (ii) on average, the atomic density is lower in the deformed specimens compared to the unloaded state, (iii) the positive atomic strain contribution

in the transverse direction is larger for the less deformed specimen for both compositions suggesting an increase of excess free volume during the early stages of deformation followed by a relaxation mechanism and (iv) the composition with the largest amount of Zr ($Zr_{65}Ni_{35}$) exhibits a less pronounced decrease of ε_{xx} with ε_m.

In Fig. 2(c), the vertical bars give the local minimum and the local maximum of ε_{yy} and ε_{xx} measured in the probed area for each specimen. The dispersion around the mean values widens with the increase of ε_m. However, there is no information on how this dispersion is spatially distributed inside the specimens. To do so, for each specimen, the spatial distribution maps of the local normalized deviation $\widetilde{\varepsilon}_{yy} = \frac{\overline{\varepsilon}_{yy} - \varepsilon_{yy}}{\overline{\varepsilon}_{yy}}$ are plotted in Fig. 3(a), with $\overline{\varepsilon}_{yy}$ the average atomic strain along y and ε_{yy} the local atomic strain. These maps show that, even if the dispersion increases (mainly because of more distant extrema), the spatial distribution remains quite homogeneous, displaying areas of similar length scale and shape for positive ($0 < \widetilde{\varepsilon}_{yy} < +0.5$, in yellow) or negative ($-0.5 < \widetilde{\varepsilon}_{yy} < 0$, in violet) values of $\widetilde{\varepsilon}_{yy}$.

Therefore, while the atomic strain along y inside the film can vary from one location to another, there is a priori no visible sign of specific spatial localization events that could be related for instance to shear bands. This confirms that the ZrNi TFMG deforms in an homogeneous way in tension before failure, at least above a length scale of the order of the probe size (200 nm). On the other hand, the major finding concerning ε_{xx}, beyond its magnitude, is its positive value. Indeed, Fig. 2(c) shows, as already indicated before, that ε_{xx} displays positive average values up to the last unbroken specimen S33. Interestingly, the vertical bars show that inside the probed area, ε_{xx} can locally reach negative values (both for S17 and S33). Figure 3(b) gives the ε_{xx} spatial distribution maps for each specimen. Only few small spots inside S17 involve local negative ε_{xx} values (blue spots), while in S33, these regions of negative ε_{xx} correspond to about 28% of the analysed area. The presence of spots with negative ε_{xx} correlates with locations corresponding to large ε_{yy} values, *i.e.* where atomic bonds are more stretched along the loading direction (bottom right of the S33 map). By extrapolating these results, we hypothesize that the next specimens (from S34 to S40, which are all broken) have thus been deformed at least slightly more than the S33 involving a structural state with an even larger amount of locations with negative ε_{xx} values, which is the atomic behaviour commonly observed in bulk metallic glasses [29, 30, 41]. This statement is further supported by the fact that in specimen S40 of the $Zr_{65}Ni_{35}$ composition, only 0.7% of the analysed area was found to display negative ε_{xx} values and it remains unbroken.

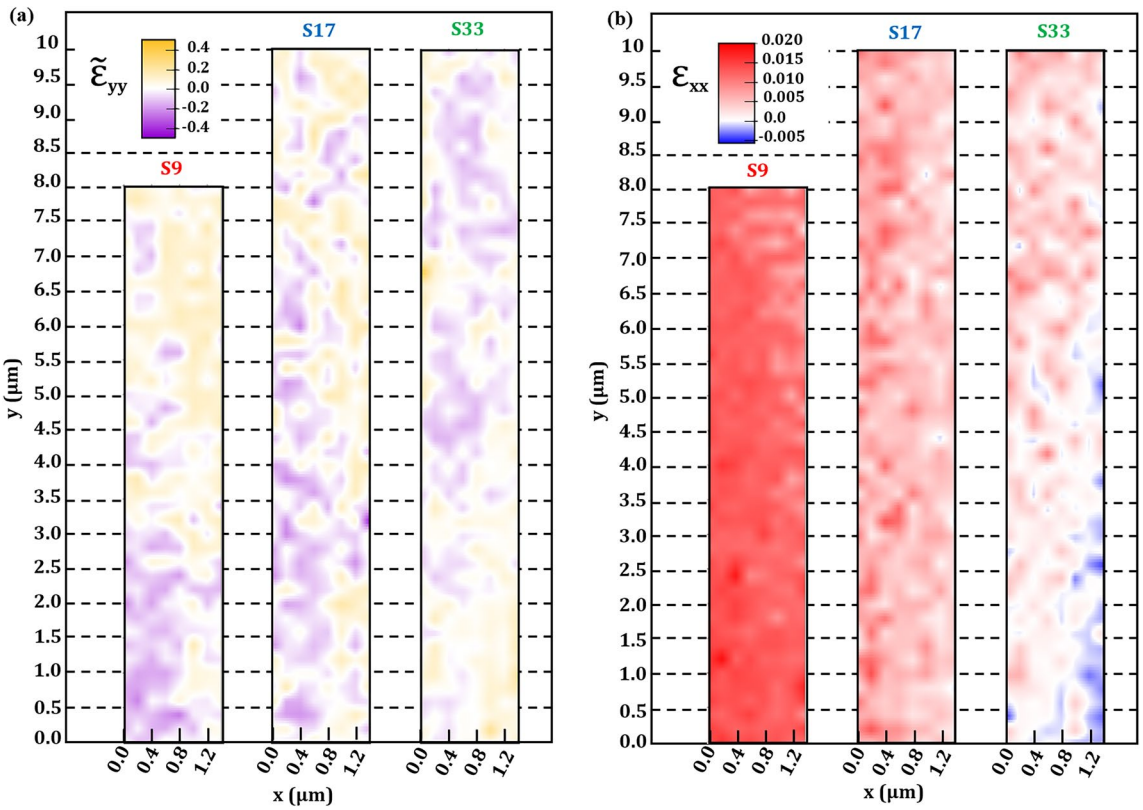

Figure 3: $Zr_{42}Ni_{58}$ spatial distribution maps of (a) the normalized deviation of the local atomic strain along the loading direction y ($\widetilde{\varepsilon}_{yy}$) and (b) the local atomic strain along the transverse direction x for S9 (1.4 × 8 μm2), S17 (1.4 × 10 μm2) and S33 (1.4 × 10 μm2) specimens.

In order to investigate deeper if this intriguing finding of transverse dilatancy in the first stage of deformation could be related to a specific pristine microstructure of the as-deposited TFMGs, a strain-temperature equivalence approach was applied on the $Zr_{65}Ni_{35}$ composition.

In situ high temperature transmission electron microscopy

An undeformed specimen and a 12% deformed specimen, taken from another series, were gradually heated in situ inside the TEM in order to track structural evolutions with temperature (from RT up to 500 °C). FFT images obtained on high-resolution HAADF-STEM images acquired at different temperatures (RT, 100 °C, 200 °C, 300 °C, 400 °C and 500 °C) before and after deformation at 12% are shown in Figs. 4 and 5, respectively. These FFTs were angularly integrated over 360° to extract the position of the scattered intensity with temperature [Fig. 6 (a) and (c)]. The maximum intensity along the ring was also extracted to track the evolution of the local order with heating (Fig. 6(b) and (d)).

This method was adopted instead of classical selected area electron diffraction in order to reveal very local phenomena associated to the nanostructured character of the ZrNi films containing Zr-rich and Ni-rich regions (Figure S2) [23].

In the undeformed sample, the maximum of intensity is initially positioned at around 2.5 $Å^{-1}$ at RT [Fig. 6(a)] in agreement with the X-ray results and NBED analysis (Fig S2). The intensity profile is almost flat [Fig. 6 (b)] suggesting the absence of any particular atomic order anisotropy inside the film after deposition and FIB milling. When the temperature is increased up to 100 °C, no change of the position of the q peak is detected in Fig. 6 (a). However, in Fig. 6(b), the orientation distribution is clearly less uniform, indicating the emergence of a nanotexture related to the emergence of some atomic order anisotropy. At 200 °C, the peak substantially shifts to lower q values revealing a significant increase of the mean interatomic distance compared to RT [Fig. 6(a)]. This important peak shift cannot be attributed to thermal expansion only as a variation of q values of only 1% is expected between RT and T_g [42]. Interestingly, this unusual large atomic expansion of the material at relatively low temperature is also accompanied by a decrease of the atomic order anisotropy compared to 100 °C with a more uniform orientation distribution in Fig. 6(b). At 300 °C, the main peak of Fig. 6(a) splits into two side peaks revealing that two distinct atomic bond lengths coexist at this temperature. The degree of atomic order anisotropy remains low at this temperature but is different when compared to 100 °C [Fig. 6(b)]. In Fig. 6(a), the vanishing of the low-q peak together with the maintained presence of the high-q peak with further annealing (at 400 °C and 500 °C) suggests that 300 °C corresponds to a transition step from

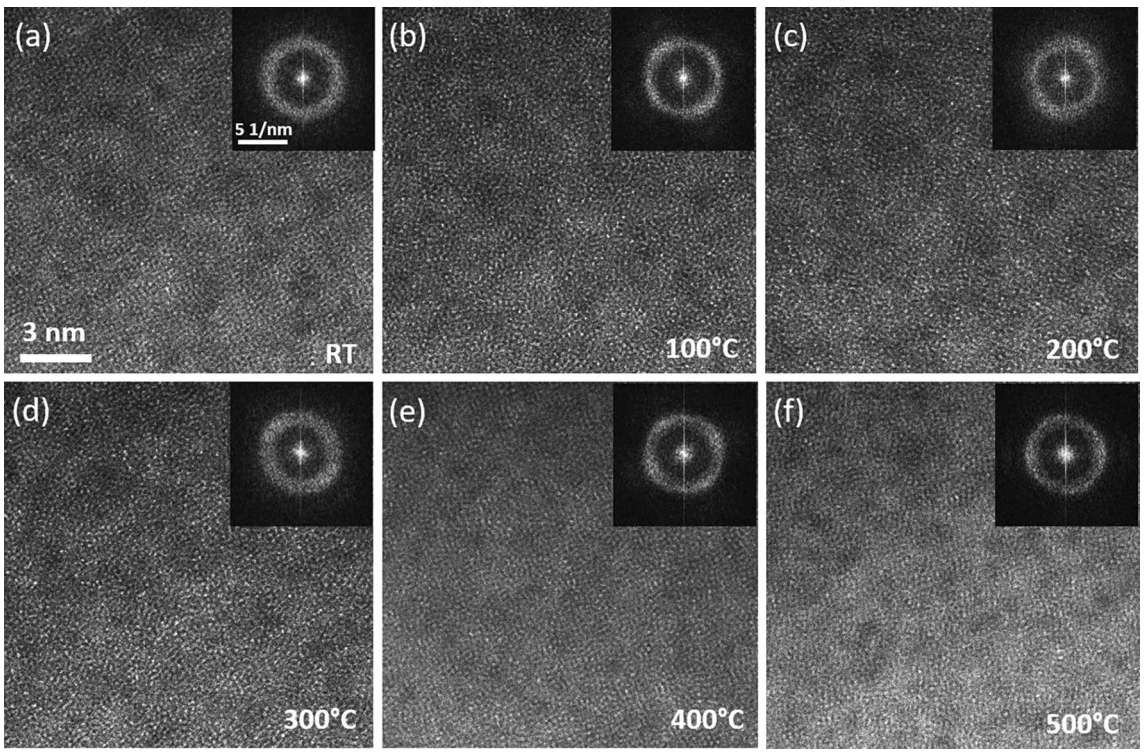

Figure 4: HAADF-STEM images acquired during annealing of a $Zr_{65}Ni_{35}$ sample from RT to 500°C before deformation. The FFT images used to produce Fig. 6 (a) and (b) in the main manuscript are shown in inset.

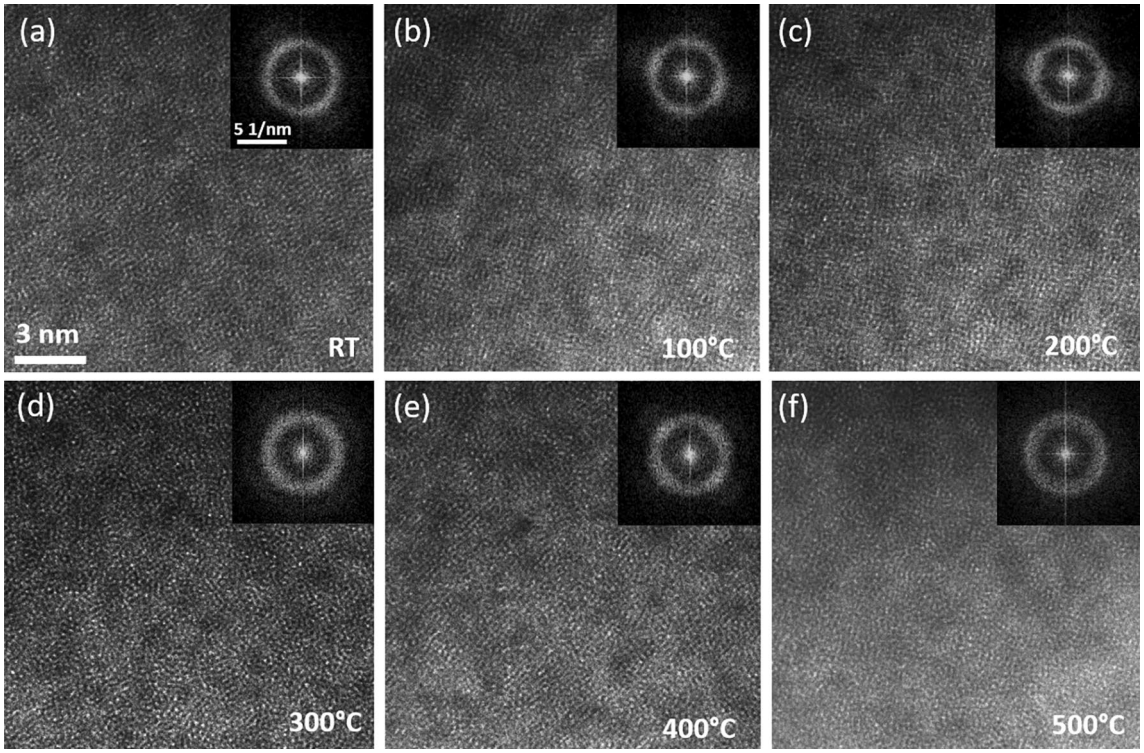

Figure 5: HAADF-STEM images acquired during annealing of a $Zr_{65}Ni_{35}$ sample from RT to 500°C after deformation up to 12%. The FFT images used to produce Fig. 6 (c) and (d) in the main manuscript are shown in inset.

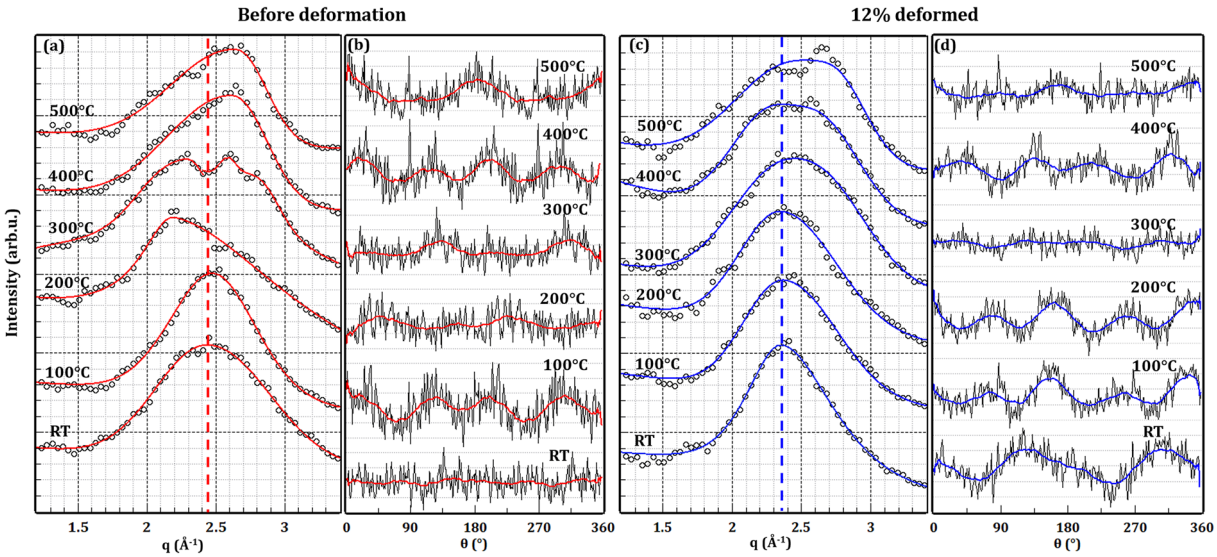

Figure 6: (a) Main peak position and (b) intensity variation along the ring as a function of temperature, before deformation. (c) Main peak position and intensity variation along the ring, as a function of temperature, after deformation. For (a) and (c), the lines are obtained by fitting the experimental data points with a Pseudo-Voigt function. For (b) and (d) , the raw curves are plotted together with the corresponding smooth curves as a guide to the eyes.

the lower temperature atomic expansion to a higher temperature atomic densification of the glass arising before reaching the glass transition temperature (T_g ~ 410 °C [43]), at which the atomic order anisotropy becomes again more obvious.

The shift of the intensity peaks with increasing temperature has already been studied by X-ray in the past [42, 44, 45], mainly to determine the thermal expansion coefficients (TEC) of metallic liquids or glasses. Such procedures have recently been contested by Gangopadhyay et al. who suggested that careful attention must be paid in the extraction of accurate quantitative TEC values as significant errors can arise due to the overlap of the partial structure factors associated to multi-element alloys [46]. Nonetheless, below the glass transition temperature and for binary systems, the direction of the shift of the principal intensity peak remains a consistent footprint of the expansion or of the contraction of the short and medium range order [45]. For instance, Yavari et al. [42] revealed by synchrotron X-ray scattering the slight shift of the first peak of the structure factor towards low-q values due to thermal expansion. Interestingly, the same procedure applied to a sample already annealed at T_g displayed a weaker peak shift. This observation is explained by the fact that the excess free volume contained in the as-cast sample was annihilated during the first heating step and does not participate to the peak shift during the second annealing.

When following a similar approach with the 12% deformed sample, striking differences are found compared to the undeformed reference specimen [Fig. 6(c) and (d)]. Indeed, the main peak remains globally at the same position from RT to 200 °C, confirming that no abnormal atomic expansion takes place. The main peak is located at lower q values compared to the undeformed sample which also suggest the presence of residual strain. Note that, in contrast with the undeformed film, clear atomic order anisotropy is observed here at RT indicating that the amorphous microstructure has undergone atomic rearrangement during deformation. Furthermore, slight changes of the atomic order anisotropy can be observed at 100 °C. No transition step is observed at 300 °C for the q peak position in Fig. 6(c). Indeed, only the high-q peak is present together with a disappearance of the atomic order anisotropy. At higher temperature (400 °C and 500 °C), a behaviour similar to the undeformed sample is found with a small shift of the main peak towards higher q values, indicating atomic densification also accompanied with the reappearance of some atomic order anisotropy. As thermal expansion is a second-order effect in terms of the magnitude of the expected thermal strain component, these results mainly show that inside the undeformed film, generation of excess volume takes place at low temperature while it does not inside a pre-deformed sample. This indicates that the capacity to generate excess volume has been exhausted in the deformed specimen during previous deformation. This is further highlighted in Fig. 7 showing the evolution of the atomic volume V_a [45, 47] as a function of annealing temperature: for the deformed sample, only a decrease of V_a is measured with the increase of the temperature.

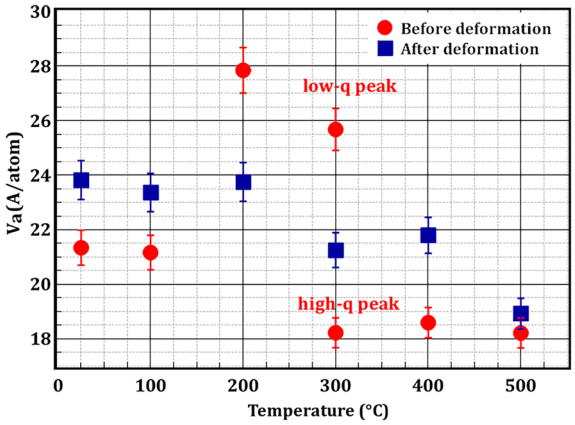

Figure 7: Evolution of the mean atomic volume V_a using the relationship $q.V_a^{0.433} = 9.3$ [47] as a function of temperature for the undeformed and deformed films.

Therefore, the TEM characterization consolidates the X-ray results shown in Fig. 2. More precisely, local atomic dilatancy occurs at the early stage of deformation (positive ε_{xx}) followed by progressive annihilation of excess free volume, as illustrated by the negative slope of ε_{xx} in Fig. 2(c) and (d). The precise nature of the underlying atomic ordering transitions is still open for exploration using atomistic simulations, but some additional elements of analysis can be proposed to shed a first light on these mechanisms as elaborated in the discussion hereafter.

Discussion

Atomic and macroscopic strain

The discrepancy between the atomic and the macroscopic strain arises from the fact that strain accommodation takes place through the activation of shear transformation zone (STZ) which potentially also involve local rotation and/or bond stretching [48] and/or exchange or rearrangement of atoms of different types [45]. In our case, the X-ray probe size remains too large to resolve potential local changes of the atomic strain at the length scale of a STZ but also at the scale of the chemical and/or atomic density heterogeneities revealed by high-resolution TEM (see Figure S2 and [23, 38]). Nonetheless, the good overall agreement between ε_a and ε_m for the specimen $Zr_{42}Ni_{58}$-S9 for instance points towards affine bond stretching as the main deformation mechanism, at least in the elastic regime. In the plastic regime, ε_a can reach relatively high values but remains always below those extracted macroscopically which is a signature of numerous permanent local atomic rearrangements impacting the macroscopic response. For $Zr_{65}Ni_{35}$, when ε_m reaches 12%, ε_a is only equal to 4% which indicates indeed large plastic strains related to STZ

activation, similar to dislocation plasticity in metals that take place with significant change in atomic spacing. To go further, the links between the observation of homogeneous dilatancy, the glass dynamics of the heterogeneous microstructure and the macroscopic ductility are addressed and discussed below.

Homogeneous dilatancy in metallic glasses revealed by elastostatic loading

While the origin of anisotropic atomic strains is a fundamental question already addressed in the field [31, 49–51], the nature of the local atomic deformation mechanisms in small scale metallic glasses remains obscure. In Chen et al. [20], both the ductility and work-hardening in 70-nm-diameter freestanding electroplated NiP metallic glass were measured. Using MD simulations, the authors explained such results throughout complex atomic reorganisation including the decrease of the atomic density in the core section of the sample especially in the elastic regime alongside the relaxation of the surface atoms. In the present work, the measurements provide only the first intensity maximum of the structure factor and the decorrelation between core and surface atoms is not possible but are in line with similar dilatation mechanisms discussed in deformed NiP nano-columns [20].

Dilatancy is a well-known deformation mechanism in granular materials and has also been reported in metallic glasses at the atomic scale [52]. Indeed, the deformation of a particularly dense or constrained amorphous atomic structure requires, throughout the activation of STZ, a temporary volume expansion under load in order to allow atomic shuffling process [3, 53]. The production of free volume generated during a STZ initiation then relaxes with time and thermal activation [54]. It is commonly assumed that such production of free volume is only localized in shear bands and potentially in the nearby surrounding matrix.

However, following the work of Park et al. [55], Ke et al. [56] showed that a MG sample submitted to a compressive elastostatic load (80% of yield stress for 12 h) deforms homogeneously (absence of shear bands) along with a decrease of density over time, i.e. with the creation of excess volume (generally called rejuvenation). These results indicated that the dilatation produced by the homogeneous deformation prevails over densification mechanisms from the hydrostatic component of the applied stress [56]. Therefore, during homogeneous flow, even at RT, free volume creation (i.e. rejuvenation) can arise even without the occurrence of shear bands. Interestingly, Greer et al. reported that elastostatic loading in tension is more effective to trigger rejuvenation than in compression [57].

In the present work, as a result of the implementation of the on-chip test method, each specimen is deformed in tension and maintained under load in a pseudo-creep test experiment (load is not fully constant over time). Therefore, in each series, the different specimens are gradually maintained at different percentage of the yield stress so that each specimen presents different levels and ratio of elastic strain, anelastic strain and viscoelastic strain (and plastic strain for those in the plastic regime). Owing to the small thickness, all specimens are deformed homogeneously [Fig. 3] and the present results suggest that transverse dilatation is favoured by elastostatic loading at small stresses [Fig. 2 and Figure S4]. As it is known that even for very low strains in the elastic regime, irreversible local atomic reorganisations can take place [58], one central question emerges about a possible intrinsic propensity of the heterogeneous pristine microstructure to favour such local reorganisation.

Role of the heterogeneous microstructure and the link with the glass dynamics

It has been shown by molecular dynamics (MD) that during elastostatic loading, the percentage of densely packed region decreases while the percentage of more loosely packed regions increases [59]. More specifically, the loading produces both the formation and the annihilation of densely packed clusters but the destruction rate is faster. This statement is closely related to the dynamics of the glass, especially to the β relaxation [60–62] that is activated under stress or annealing (at relativity low T below T_g) and is expected to play an important role in dictating the deformation of MGs [63, 64]. Indeed, theoretical models suggest that the β-relaxation takes place through the translational motion of atoms localized in loosely packed regions [65] and is therefore linked to the excess free volume of flow defects: β-relaxation and STZ have, for instance, similar activation energy [57]. This scheme certainly assumes that β-relaxation intrinsically correlates with the presence of structural heterogeneities in MGs. Indeed, Zhu et al. recently demonstrated an intrinsic correlation between β-relaxation and spatial heterogeneity in MGs using amplitude-modulation dynamic atomic force microscopy (AM-AFM) [66].

Similarly, the TEM results shown here shed new light on this phenomenon: the presence of two coexisting distinct atomic bond lengths in the glass at 300 °C [Figs. 6(a), 7] might be linked to the structural heterogeneities. Indeed, the less dense Zr-rich clusters are more prone to undergo atomic rearrangement, and therefore β relaxation, compared to the denser Ni-rich clusters during annealing (and upon deformation). This transition step at 300 °C might constitute first-of-kind experimental evidence of a two-step β-relaxation in a highly heterogeneous amorphous structure. The following scenario can be proposed. After large and homogeneous dilatation by generation of free volumes at 200 °C, the less dense Zr-rich clusters start to densify at 300 °C,

while the Ni-rich clusters are not affected by the β-relaxation. At 400 °C, atomic mobility expands to the Ni-rich domains leading to a more homogenous densification of the glass (α-relaxation) which continues at 500 °C. Remarkably, the absence of this transition in the deformed sample [Fig. 6(c)] confirms that the mechanism described above similarly occurred during deformation. This scenario is also consistent with the observed outcomes of studies on metallic glasses investigating shear-induced chemical segregation [67, 68] which is, as for dilatancy, a comparable feature already identified during the flow of granular materials. The presence of large (Zr) and small (Ni) atoms could lead to element segregation during local shearing and could at some point lead to the presence of two characteristic atomic bond lengths, similarly to what is observed during thermal treatment but throughout deformation. This particular point could also be a topic of investigation in the future.

Structural-and size-enhanced ductility by PVD

The dilatancy mechanism discussed above, while interesting per se for its partly unexpected nature, may also be one more important element to add in the global understanding of the phenomenology of the plastic deformation and ductility of MG. It is shown here that in the ductile heterogeneous ZrNi metallic glass thin films, deformation and thermal annealing similarly lead to the homogeneous creation of free volume (i.e. rejuvenation) followed by localized relaxation mechanisms. Our results support the findings made in other studies showing that rejuvenated metallic glasses [69, 70] and/or metallic glasses (as well as nanoglasses) with promoted β-relaxation exhibit enhanced microscale tensile plasticity [60, 64, 71, 72]. It is believed that the processing of the metallic glass thin films by physical vapour deposition is at the origin of both the extrinsic and intrinsic features resulting in the enhancement of ductility. Indeed, the sputtering process can produce

- films free of defects (porosities, crystalline inclusions, etc.) together with a low surface roughness, all favourable features promoting ductility [9, 19],
- films with very low thickness that prevent the formation of mature shear bands and therefore promoting homogeneous deformation [9, 38],
- films with very dense packing structure [73] that are therefore more likely to display atomic dilatancy during homogeneous deformation, producing free volume [56, 57] in order to accommodate deformation and/or thermal strain,
- films with highly heterogeneous structures, more prone to β-relaxation activation [66], together with limited STZ percolation [23, 34]

The last two points, covered by the findings of this work, support the scenario into which the presence of the loosely packed regions (here Zr-rich clusters), which are favoured by the homogeneous dilatancy, are fertile sites for the activation of STZs as well as β-relaxations. At the same time, the denser Ni-rich clusters act as strong inclusions that retard catastrophic shear banding by hindering the percolation of the STZ which also restrains the β-relaxation inside the loosely packed region. With this picture, the difference in ductility between the two compositions can be explained by the increase of Ni content between the $Zr_{65}Ni_{35}$ and the $Zr_{42}Ni_{58}$ compositions leading to a decrease of the amount of Zr-rich soft regions and leads to a change of their spatial distribution, limiting both the nucleation of STZ and the occurrence of β-relaxation and thus limit plastic flow. A correlated finding from this work concerns the magnitude of dilatation during homogeneous deformation at RT in the ZrNi amorphous thin films which seems to be a good indicator of the facility to activate β-relaxation. This is a promising approach to mechanically probe a metallic glass dynamic even possibly in bulk samples.

Complementary studies to go further involve more in-depth on-chip tests (including the recording of strain evolution over time and/or unloading experiments) and the use of atomistic calculation to investigate the complex evolution of the atomic order anisotropy [Fig. 6] reflecting transitions between different metastable glassy phases [74]. Advanced TEM investigations are also needed to probe the evolution of the local order and the atomic strain directly inside the Ni-rich and Zr-rich clusters. For instance, the use of nanobeam electronic diffraction in metallic glass thin films designed with well-controlled density/chemical heterogeneities arranged in nanolayered structure [75] is a promising way to facilitate the probe of nanoscale single glassy phases and interfaces.

Conclusion

ZrNi 360-nm-thick freestanding films deformed in tension were characterized with a highly focussed X-ray synchrotron beam along with high-resolution TEM in situ heating measurements. The main finding of the work is the unveiling of the room temperature development of atomic and macroscopic homogeneous dilatancy under tension inside TFMG. A two-step temperature-driven transition between a structural state of low density involving the redistribution of free volumes to a more relaxed state with densification is also observed. Such thermal dependency is not observed in deformed films into which only atomic densification is detected. It confirms the capacity of the TFMG to develop strain- and temperature-induced atomic dilatancy

without localisation is an intrinsic property of the as-deposited pristine microstructure of the glass. It is believed that the heterogeneous structure composed of very small (2 – 3 nm) Zr-rich and Ni-rich domains plays a key role in this mechanism and in setting the ductility of the systems. The loosely packed Zr-rich domains must be prone to developed atomic dilatancy throughout STZ nucleation as well as to further undergo β-relaxation, whereas Ni-rich domains prevent the percolation of STZ, all these features being favourable to avoid strain localisation.

Materials and methods

Freestanding ZrNi TFMG preparation and mechanical characterization

ZrNi TFMG have been deposited with two different compositions (i.e. $Zr_{42}Ni_{58}$ or $Zr_{65}Ni_{35}$ At.%) and a thickness of 360 nm using an Alliance Concept AC450 DC-magnetron sputtering machine (target-sample distance: 10 cm, base pressure < 4.10^{-5} Pa, Ar pressure: 0.3 Pa and DC-power 300 W). The specific target is made of very pure Zr with an adaptable number of rectangular Ni inserts to reach the desired composition.

The mechanical response has been determined using the on-chip nanomechanical testing technique developed at UCLouvain [35, 36]. Each $Zr_{42}Ni_{58}$ or $Zr_{65}Ni_{35}$ dogbone TFMG specimen overlaps a Si_3N_4 actuator beam containing large tensile residual stress (~ 1 GPa). Both beams are patterned by lithography. These test structures (Si_3N_4 actuators + ZrNi specimens) lie on a Si (001) substrate. When the Si material under the test structures is chemically etched, the test structures are released from the substrate with the actuators pulling on the TFMG specimens until load equilibrium is reached [Fig. 1(a)]. Different equilibrium states, *i.e.* different deformed states, are obtained by varying the actuator length. In the present study, series of 40 TFMG specimens (2 µm in width, 50 µm in length and 360 nm in thickness) were released, each specimen providing one point of the stress–strain response [Fig. 1(b)]. The Si etching step was performed during 10 min in a 10% vol. TMAH (tetramethylammonium hydroxide):H2O solution at 80 °C leading to an under-etching equal to 10 µm [43]. After release, the displacement between the fixed and the moving cursors is measured by scanning electron microscopy (SEM). Subsequently, a post-treatment of the mechanical and geometrical parameters gives access to the tensile stress–strain response of the material (Fig S1). For extended details on the on-chip test method, TFMG processing and macroscopic evaluation of the stress–strain curves, the reader is referred to earlier studies [9, 35] as well as to the Supplementary Materials.

Synchrotron X-ray scattering experiments

The synchrotron X-ray scattering experiments were carried out at the ID01 beamline at ESRF (European Synchrotron Research Facility). The beam energy was set to 19.6 keV with a multilayer mirror at an optimized flux and focussed throughout Kirkpatrick-Baez (KB) mirrors with a spot size of 200×200 nm^2 in the vertical (y) and horizontal (x) directions, respectively. The transmitted signal is recorded with a 2D Maxipix 2×2 detector developed at the ESRF and composed of 4 chips of 256×256 pixels each with a pixel size of 55 µm. The Si die supporting the series of test specimens was mounted vertically [Fig. 1(c)]. The mapped area was equal to 1.4×10 µm^2 recorded with a mesh size of the order of the spot size in both directions with an exposure time of 10 s. This leads to a set of data composed of 350 images recorded in about 2 h (acquisition time + dead times) for each specimen. The unloaded reference state (Fig S1) was probed using the same procedure over 35 images. The raw images were further corrected from the Si background signal by subtraction of the scattered signal recorded outside but nearby the edge of the corresponding specimen. An example image is shown in Fig. 1(c). The reciprocal space scale was calibrated using the (111) ring from a Si powder probed in the exact same position and acquisition conditions. Subsequently, the intensity of the ring in each image is fitted using a 2D elliptical function to extract the length of the main axis and determine the magnitude of the atomic strain along the principal directions (x and y).

In situ high-resolution transmission electron microscopy experiments

An as-deposited and a 12% deformed $Zr_{65}Ni_{35}$ TFMGs were annealed using the single tilt Wildfire in situ TEM heating holder from DENSsolutions.Inc. This instrument enables high-resolution TEM characterizations at high temperature (up to 1300 °C) with optimum stability, thanks to micro-electro-mechanical systems as shown in Fig. 1(d). Cross-sectional TEM foils were prepared using FIB from as-deposited ZrNi TFMGs and from a specimen deformed up to 12% (taken from another series) using the lift out method in a FEI Helios NanoLab 650 FIB/SEM dual-beam instrument. A Pt layer was deposited in two steps—by electron beam, then by ion beam—in order to minimize FIB damage at the sample surface. An ion beam of 2 kV/0.2 nA was employed for final thinning and to minimize defects generated during high voltage FIB thinning on both sides of the sample after mounting on the heating chip. High-resolution scanning TEM (STEM) imaging was performed on a FEI Titan "cubed" microscope, operated at a 300 kV acceleration

voltage and equipped with both TEM and STEM aberration correctors.

High-resolution high-angle-annular-dark field scanning TEM (HAADF-STEM) images were acquired using a convergence semi-angle α of 22 mrad and 25 pA probe current, the ADF inner acceptance angle β and the EELS acceptance angle were both equal to 28 mrad. All high-resolution images have been acquired on regions with thickness around 15 nm (in the *yz* plan) as revealed by electron energy loss spectroscopy (EELS), see [23]. Figure 1(e) exhibits an example of a high-resolution HAADF-STEM image of the $Zr_{65}Ni_{35}$ TFMG. It shows nanoscale heterogeneities involving bright and dark nanodomains with a characteristic length scale of ~ 2–3 nm. Such features have been identified by EELS as dense (bright) Ni-rich clusters embedded in Zr-rich (dark) clusters with lower atomic density, see Fig S2 in SupMat and [23]. In the present work, nanobeam electron diffraction (NBED) patterns recorded on the heterogeneities with a probe size of 1.2 nm have shown that the Ni-rich clusters exhibit a smaller average atomic spacing compared to the Zr-rich clusters (Fig S2). Figure 1(f) shows Fast Fourier transforms extracted from the image in Fig. 1(e). Changes of nano-FFTs images with the temperature in the as-deposited and the deformed films have been analysed (position and intensity variation along the ring) in order to unravel the effect of temperature on the evolution of the average atomic spacing and atomic order (more details are given in the next section).

Acknowledgments

We acknowledge the European Synchrotron Radiation Facility for provision of synchrotron radiation facilities and we would like to thank Tao Zhou for assistance in using beamline ID01 as well as all the ID01 staff. The authors would like to deeply acknowledge R. Tuyaerts (UCL, Belgium), A. Crahay, E. Tooten and S. Faniel (WinFab, Belgium), the ID01 beamline staff as well as F. Gustavo (PTA) for their great help concerning this study. Stijn Van den Broeck (EMAT, Antwerp, Belgium) is also acknowledged for the FIB sample preparation.

Author contributions

R. Daudin processed the samples, performed the on-chip tests, carried out the synchrotron X-ray experiment, analysed the data and wrote the paper; H. Idrissi performed the in situ HR-TEM measurements, analysed and discussed the data, wrote the paper; M. Coulombier processed the samples, performed the on-chip tests and reviewed the paper; P. Lhuissier developed the code to analyse the X-ray data and reviewed the paper; A. Béché performed the NBED experiments of Fig S2 in the SM; J. Verbeeck and D. Schryvers participated to the analysis and the discussion of the TEM results; M. Ghidelli processed the samples and reviewed the paper; J.P. Raskin initiated the work and reviewed the paper; J.-J. Blandin supervised the work and reviewed the paper; T.U. Schülli conducted the synchrotron X-ray experiment and reviewed the paper; T. Pardoen initiated and supervised the work, discussed the results, wrote some parts and reviewed the paper.

Funding

H. Idrissi is mandated by the Belgian National Fund for Scientific Research (FSR-FNRS). A. Béché received funding from the European Union under grant agreement No 823717 ESTEEM3. This work was supported by the FNRS under Grant CDR – J.0113.20 as well as by the "MOVE-IN" Louvain transnational programme.

Data availability

The data that support the findings of this study are available from the corresponding authors upon reasonable request.

Declarations

Competing interest Not applicable.

References

1. A.L. Greer, Y.Q. Cheng, E. Ma, Shear bands in metallic glasses. Mater. Sci. Eng. R. Rep. **74**, 71–132 (2013). https://doi.org/10.1016/j.mser.2013.04.001
2. M.D. Demetriou, M.E. Launey, G. Garrett, J.P. Schramm, D.C. Hofmann, W.L. Johnson, R.O. Ritchie, A damage-tolerant glass. Nat. Mater. **10**, 123–128 (2011). https://doi.org/10.1038/nmat2930
3. T.C. Hufnagel, C.A. Schuh, M.L. Falk, Deformation of metallic glasses: recent developments in theory, simulations, and experiments. Acta Mater. **109**, 375–393 (2016). https://doi.org/10.1016/j.actamat.2016.01.049
4. C.A. Volkert, A. Donohue, F. Spaepen, Effect of sample size on deformation in amorphous metals. J. Appl. Phys. **103**, 083539 (2008). https://doi.org/10.1063/1.2884584
5. Y. Shi, Size-dependent mechanical responses of metallic glasses. Int. Mater. Rev. **64**, 163–180 (2019). https://doi.org/10.1080/09506608.2018.1476079
6. J.R. Greer, JTh.M. De Hosson, Plasticity in small-sized metallic systems: Intrinsic versus extrinsic size effect. Prog. Mater. Sci. **56**, 654–724 (2011). https://doi.org/10.1016/j.pmatsci.2011.01.005
7. L. Tian, X.-L. Wang, Z.-W. Shan, Mechanical behavior of micro-nanoscaled metallic glasses. Mater. Res. Lett. **4**, 63–74 (2016). https://doi.org/10.1080/21663831.2015.1124298

8. K.S. Nakayama, Y. Yokoyama, T. Ono, M.W. Chen, K. Akiyama, T. Sakurai, A. Inoue, Controlled formation and mechanical characterization of metallic glassy nanowires. Adv. Mater. **22**, 872–875 (2010). https://doi.org/10.1002/adma.200902295
9. M. Ghidelli, H. Idrissi, S. Gravier, J.-J. Blandin, J.-P. Raskin, D. Schryvers, T. Pardoen, Homogeneous flow and size dependent mechanical behavior in highly ductile Zr 65 Ni 35 metallic glass films. Acta Mater. **131**, 246–259 (2017). https://doi.org/10.1016/j.actamat.2017.03.072
10. D. Tönnies, R. Maaß, C.A. Volkert, Room temperature homogeneous ductility of micrometer-sized metallic glass. Adv. Mater. **26**, 5715–5721 (2014). https://doi.org/10.1002/adma.201401123
11. D. Jang, J.R. Greer, Transition from a strong-yet-brittle to a stronger-and-ductile state by size reduction of metallic glasses. Nature Mater. **9**, 215–219 (2010). https://doi.org/10.1038/nmat2622
12. L. Tian, Y.-Q. Cheng, Z.-W. Shan, J. Li, C.-C. Wang, X.-D. Han, J. Sun, E. Ma, Approaching the ideal elastic limit of metallic glasses. Nat. Commun. **3**, 1–6 (2012). https://doi.org/10.1038/ncomms1619
13. R. Liontas, M. Jafary-Zadeh, Q. Zeng, Y.-W. Zhang, W.L. Mao, J.R. Greer, Substantial tensile ductility in sputtered Zr-Ni-Al nano-sized metallic glass. Acta Mater. **118**, 270–285 (2016). https://doi.org/10.1016/j.actamat.2016.07.050
14. J.H. Luo, F.F. Wu, J.Y. Huang, J.Q. Wang, S.X. Mao, Superelongation and atomic chain formation in nanosized metallic glass. Phys. Rev. Lett. **104**, 215503 (2010). https://doi.org/10.1103/PhysRevLett.104.215503
15. H. Guo, P.F. Yan, Y.B. Wang, J. Tan, Z.F. Zhang, M.L. Sui, E. Ma, Tensile ductility and necking of metallic glass. Nature Mater. **6**, 735–739 (2007). https://doi.org/10.1038/nmat1984
16. O.V. Kuzmin, Y.T. Pei, C.Q. Chen, J.T.M. De Hosson, Intrinsic and extrinsic size effects in the deformation of metallic glass nanopillars. Acta Mater. **60**, 889–898 (2012). https://doi.org/10.1016/j.actamat.2011.11.023
17. D.J. Magagnosc, R. Ehrbar, G. Kumar, M.R. He, J. Schroers, D.S. Gianola, Tunable tensile ductility in metallic glasses. Sci Rep (2013). https://doi.org/10.1038/srep01096
18. L. Tian, Z.-W. Shan, E. Ma, Ductile necking behavior of nanoscale metallic glasses under uniaxial tension at room temperature. Acta Mater. **61**, 4823–4830 (2013). https://doi.org/10.1016/j.actamat.2013.05.001
19. S. Adibi, P.S. Branicio, R. Liontas, D.Z. Chen, J.R. Greer, D.J. Srolovitz, S.P. Joshi, Surface roughness imparts tensile ductility to nanoscale metallic glasses. Extreme Mech Lett **5**, 88–95 (2015). https://doi.org/10.1016/j.eml.2015.08.004
20. D.Z. Chen, X.W. Gu, Q. An, W.A. Goddard, J.R. Greer, Ductility and work hardening in nano-sized metallic glasses. Appl. Phys. Lett. **106**, 061903 (2015). https://doi.org/10.1063/1.4907773
21. A. Dubach, R. Raghavan, J.F. Löffler, J. Michler, U. Ramamurty, Micropillar compression studies on a bulk metallic glass in different structural states. Scripta Mater. **60**, 567–570 (2009). https://doi.org/10.1016/j.scriptamat.2008.12.013
22. J. Luo, P. Keblinski, Y. Shi, A model metallic glass exhibits size-independent tensile ductility. Acta Mater. **103**, 587–594 (2016). https://doi.org/10.1016/j.actamat.2015.10.029
23. H. Idrissi, M. Ghidelli, A. Béché, S. Turner, S. Gravier, J.-J. Blandin, J.-P. Raskin, D. Schryvers, T. Pardoen, Atomic-scale viscoplasticity mechanisms revealed in high ductility metallic glass films. Sci. Rep. **9**, 13426 (2019). https://doi.org/10.1038/s41598-019-49910-7
24. J.C. Qiao, Q. Wang, J.M. Pelletier, H. Kato, R. Casalini, D. Crespo, E. Pineda, Y. Yao, Y. Yang, Structural heterogeneities and mechanical behavior of amorphous alloys. Prog. Mater. Sci. **104**, 250–329 (2019). https://doi.org/10.1016/j.pmatsci.2019.04.005
25. F. Zhu, S. Song, K.M. Reddy, A. Hirata, M. Chen, Spatial heterogeneity as the structure feature for structure–property relationship of metallic glasses. Nat. Commun. **9**, 3965 (2018). https://doi.org/10.1038/s41467-018-06476-8
26. E. Ma, J. Ding, Tailoring structural inhomogeneities in metallic glasses to enable tensile ductility at room temperature. Mater. Today **19**, 568–579 (2016). https://doi.org/10.1016/j.mattod.2016.04.001
27. C. Gammer, J. Kacher, C. Czarnik, O.L. Warren, J. Ciston, A.M. Minor, Local and transient nanoscale strain mapping during in situ deformation. Appl. Phys. Lett. **109**, 081906 (2016). https://doi.org/10.1063/1.4961683
28. H. Sheng, D. Şopu, S. Fellner, J. Eckert, C. Gammer, Mapping shear bands in metallic glasses: from atomic structure to bulk dynamics. Phys. Rev. Lett. **128**, 245501 (2022). https://doi.org/10.1103/PhysRevLett.128.245501
29. H.F. Poulsen, J.A. Wert, J. Neuefeind, V. Honkimäki, M. Daymond, Measuring strain distributions in amorphous materials. Nat. Mater. **4**, 33–36 (2004). https://doi.org/10.1038/nmat1266
30. J. Das, M. Boström, N. Mattern, Å. Kvick, A.R. Yavari, A.L. Greer, J. Eckert, Plasticity in bulk metallic glasses investigated via the strain distribution. Phys. Rev. B **76**, 092203 (2007). https://doi.org/10.1103/PhysRevB.76.092203
31. U.K. Vempati, Length-scale dependence of elastic strain from scattering measurements in metallic glasses. Phys. Rev. B (2012). https://doi.org/10.1103/PhysRevB.85.214201
32. S. Scudino, R.N. Shahid, B. Escher, M. Stoica, B.S. Li, J.J. Kruzic, Mapping the cyclic plastic zone to elucidate the mechanisms of crack tip deformation in bulk metallic glasses. Appl. Phys. Lett. **110**, 081903 (2017). https://doi.org/10.1063/1.4977001
33. S. Scudino, D. Şopu, Strain distribution across an individual shear band in real and simulated metallic glasses. Nano Lett. **18**, 1221–1227 (2018). https://doi.org/10.1021/acs.nanolett.7b04816
34. S. Scudino, J.J. Bian, H.S. Shahabi, D. Şopu, J. Sort, J. Eckert, G. Liu, Ductile bulk metallic glass by controlling structural

heterogeneities. Sci. Rep. **8**, 9174 (2018). https://doi.org/10.1038/s41598-018-27285-5

35. M. Coulombier, G. Guisbiers, M.-S. Colla, R. Vayrette, J.-P. Raskin, T. Pardoen, On-chip stress relaxation testing method for freestanding thin film materials. Rev. Sci. Instrum. **83**, 105004 (2012). https://doi.org/10.1063/1.4758288
36. S. Gravier, M. Coulombier, A. Safi, N. André, A. Boé, J.-P. Raskin, T. Pardoen, New on-chip nanomechanical testing laboratory—applications to aluminum and polysilicon thin films. J. Microelectromech. Syst. **18**, 555–569 (2009). https://doi.org/10.1109/JMEMS.2009.2020380
37. S.J. Leake, G.A. Chahine, H. Djazouli, T. Zhou, C. Richter, J. Hilhorst, L. Petit, M.-I. Richard, C. Morawe, R. Barrett, L. Zhang, R.A. Homs-Regojo, V. Favre-Nicolin, P. Boesecke, T.U. Schülli, The Nanodiffraction beamline ID01/ESRF: a microscope for imaging strain and structure. J Synchrotron Rad **26**, 571–584 (2019). https://doi.org/10.1107/S160057751900078X
38. M. Ghidelli, S. Gravier, J.-J. Blandin, P. Djemia, F. Mompiou, G. Abadias, J.-P. Raskin, T. Pardoen, Extrinsic mechanical size effects in thin ZrNi metallic glass films. Acta Mater. **90**, 232–241 (2015). https://doi.org/10.1016/j.actamat.2015.02.038
39. M. Ghidelli, S. Gravier, J.-J. Blandin, T. Pardoen, J.-P. Raskin, F. Mompiou, Compositional-induced structural change in ZrxNi100−x thin film metallic glasses. J. Alloy. Compd. **615**, S348–S351 (2014). https://doi.org/10.1016/j.jallcom.2013.12.054
40. Y. Huang, J.C. Khong, T. Connolley, J. Mi, The onset of plasticity of a Zr-based bulk metallic glass. Int. J. Plast. **60**, 87–100 (2014). https://doi.org/10.1016/j.ijplas.2014.05.003
41. H. Shakur Shahabi, S. Scudino, I. Kaban, M. Stoica, U. Rütt, U. Kühn, J. Eckert, Structural aspects of elasto-plastic deformation of a Zr-based bulk metallic glass under uniaxial compression. Acta Materi. **95**, 30–36 (2015). https://doi.org/10.1016/j.actamat.2015.05.011
42. A.R. Yavari, A.L. Moulec, A. Inoue, N. Nishiyama, N. Lupu, E. Matsubara, W.J. Botta, G. Vaughan, M.D. Michiel, Å. Kvick, Excess free volume in metallic glasses measured by X-ray diffraction. Acta Mater. **53**, 1611–1619 (2005). https://doi.org/10.1016/j.actamat.2004.12.011
43. M. Ghidelli, Size dependent mechanical behavior of Zr-Ni thin metallic glass films, PhD Thesis, Université Grenoble Alpes, 2015. https://tel.archives-ouvertes.fr/tel-01310217/document (accessed March 13, 2019).
44. A.H. Taghvaei, H. Shakur Shahabi, J. Bednarčik, J. Eckert, Inhomogeneous thermal expansion of metallic glasses in atomic-scale studied by *in-situ* synchrotron X-ray diffraction. J. Appl. Phys. **117**, 044902 (2015). https://doi.org/10.1063/1.4906552
45. X. Tong, G. Wang, Z.H. Stachurski, J. Bednarčík, N. Mattern, Q.J. Zhai, J. Eckert, Structural evolution and strength change of a metallic glass at different temperatures. Sci. Rep. **6**, 30876 (2016). https://doi.org/10.1038/srep30876
46. A.K. Gangopadhyay, K.F. Kelton, A re-evaluation of thermal expansion measurements of metallic liquids and glasses from x-ray scattering experiments. J. Chem. Phys. **148**, 204509 (2018). https://doi.org/10.1063/1.5032319
47. D. Ma, A.D. Stoica, X.-L. Wang, Power-law scaling and fractal nature of medium-range order in metallic glasses. Nat. Mater. **8**, 30–34 (2009). https://doi.org/10.1038/nmat2340
48. A.J.G. Lunt, P. Chater, A.M. Korsunsky, On the origins of strain inhomogeneity in amorphous materials. Sci Rep (2018). https://doi.org/10.1038/s41598-018-19900-2
49. R.T. Ott, M.J. Kramer, M.F. Besser, D.J. Sordelet, High-energy X-ray measurements of structural anisotropy and excess free volume in a homogenously deformed Zr-based metallic glass. Acta Mater. **54**, 2463–2471 (2006). https://doi.org/10.1016/j.actamat.2006.01.026
50. M.J. Kramer, R.T. Ott, D.J. Sordelet, Anisotropic atomic structure in a homogeneously deformed metallic glass. J. Mater. Res. **22**, 382–388 (2007). https://doi.org/10.1557/jmr.2007.0044
51. Y.H. Sun, A. Concustell, M.A. Carpenter, J.C. Qiao, A.W. Rayment, A.L. Greer, Flow-induced elastic anisotropy of metallic glasses. Acta Mater. **112**, 132–140 (2016). https://doi.org/10.1016/j.actamat.2016.04.022
52. X. Sun, G. Ding, G. Mo, L.H. Dai, M.Q. Jiang, Dilatancy signatures of amorphous plasticity probed by X-ray synchrotron radiation. Intermetallics **107**, 34–38 (2019). https://doi.org/10.1016/j.intermet.2019.01.009
53. A.S. Argon, Plastic deformation in metallic glasses. Acta Metall. **27**, 47–58 (1979). https://doi.org/10.1016/0001-6160(79)90055-5
54. E.R. Homer, Examining the initial stages of shear localization in amorphous metals. Acta Mater. **63**, 44–53 (2014). https://doi.org/10.1016/j.actamat.2013.09.050
55. K.-W. Park, C.-M. Lee, M. Wakeda, Y. Shibutani, M.L. Falk, J.-C. Lee, Elastostatically induced structural disordering in amorphous alloys. Acta Mater. **56**, 5440–5450 (2008). https://doi.org/10.1016/j.actamat.2008.07.033
56. H.B. Ke, P. Wen, H.L. Peng, W.H. Wang, A.L. Greer, Homogeneous deformation of metallic glass at room temperature reveals large dilatation. Scripta Mater. **64**, 966–969 (2011). https://doi.org/10.1016/j.scriptamat.2011.01.047
57. A.L. Greer, Y.H. Sun, Stored energy in metallic glasses due to strains within the elastic limit. Philos. Mag. **96**, 1643–1663 (2016). https://doi.org/10.1080/14786435.2016.1177231
58. J.C. Ye, J. Lu, C.T. Liu, Q. Wang, Y. Yang, Atomistic free-volume zones and inelastic deformation of metallic glasses. Nature Mater. **9**, 619–623 (2010). https://doi.org/10.1038/nmat2802
59. C.-M. Lee, K.-W. Park, B.-J. Lee, Y. Shibutani, J.-C. Lee, Structural disordering of amorphous alloys: a molecular dynamics analysis. Scripta Mater. **61**, 911–914 (2009). https://doi.org/10.1016/j.scriptamat.2009.07.032

60. W.H. Wang, Dynamic relaxations and relaxation-property relationships in metallic glasses. Prog. Mater. Sci. **106**, 100561 (2019). https://doi.org/10.1016/j.pmatsci.2019.03.006
61. K.L. Ngai, S. Capaccioli, M. Paluch, L. Wang, Clarifying the nature of the Johari-Goldstein β-relaxation and emphasising its fundamental importance. Philios. Mag. **100**, 2596–2613 (2020). https://doi.org/10.1080/14786435.2020.1781276
62. Y. Sun, S.-X. Peng, Q. Yang, F. Zhang, M.-H. Yang, C.-Z. Wang, K.-M. Ho, H.-B. Yu, Predicting complex relaxation processes in metallic glass. Phys. Rev. Lett. **123**, 105701 (2019). https://doi.org/10.1103/PhysRevLett.123.105701
63. W.H. Wang, Correlation between relaxations and plastic deformation, and elastic model of flow in metallic glasses and glass-forming liquids. J. Appl. Phys. **110**, 053521 (2011). https://doi.org/10.1063/1.3632972
64. H.B. Yu, X. Shen, Z. Wang, L. Gu, W.H. Wang, H.Y. Bai, Tensile plasticity in metallic glasses with pronounced beta relaxations. Phys. Rev. Lett. **108**, 015504 (2012). https://doi.org/10.1103/PhysRevLett.108.015504
65. G.P. Johari, Localized molecular motions of β-relaxation and its energy landscape. J. Non-Cryst. Solids **307–310**, 317–325 (2002). https://doi.org/10.1016/S0022-3093(02)01491-6
66. F. Zhu, H.K. Nguyen, S.X. Song, D.P.B. Aji, A. Hirata, H. Wang, K. Nakajima, M.W. Chen, Intrinsic correlation between β-relaxation and spatial heterogeneity in a metallic glass. Nat. Commun. **7**, 11516 (2016). https://doi.org/10.1038/ncomms11516
67. Y. Rakita, J.L. Hart, P.P. Das, S. Shahrezaei, D.L. Foley, S.N. Mathaudhu, S. Nicolopoulos, M.L. Taheri, S.J.L. Billinge, Mapping structural heterogeneity at the nanoscale with scanning nano-structure electron microscopy (SNEM). Acta Mater. **242**, 118426 (2023). https://doi.org/10.1016/j.actamat.2022.118426
68. D.V. Louzguine-Luzgin, A.S. Trifonov, Y.P. Ivanov, A.K.A. Lu, A.V. Lubenchenko, A.L. Greer, Shear-induced chemical segregation in a Fe-based bulk metallic glass at room temperature. Sci. Rep. **11**, 13650 (2021). https://doi.org/10.1038/s41598-021-92907-4
69. S.V. Ketov, Y.H. Sun, S. Nachum, Z. Lu, A. Checchi, A.R. Beraldin, H.Y. Bai, W.H. Wang, D.V. Louzguine-Luzgin, M.A. Carpenter, A.L. Greer, Rejuvenation of metallic glasses by non-affine thermal strain. Nature **524**, 200–203 (2015). https://doi.org/10.1038/nature14674
70. J. Pan, Y.X. Wang, Q. Guo, D. Zhang, A.L. Greer, Y. Li, Extreme rejuvenation and softening in a bulk metallic glass. Nat. Commun. **9**, 560 (2018). https://doi.org/10.1038/s41467-018-02943-4
71. Z. Wang, W.-H. Wang, Flow units as dynamic defects in metallic glassy materials. Natl. Sci. Rev. **6**, 304–323 (2019). https://doi.org/10.1093/nsr/nwy084
72. Q. Wang, S.T. Zhang, Y. Yang, Y.D. Dong, C.T. Liu, J. Lu, Unusual fast secondary relaxation in metallic glass. Nat. Commun. **6**, 7876 (2015). https://doi.org/10.1038/ncomms8876
73. Y. Sun, A. Concustell, A.L. Greer, Thermomechanical processing of metallic glasses: extending the range of the glassy state. Nat. Rev. Mater. (2016). https://doi.org/10.1038/natrevmats.2016.39
74. H.W. Sheng, H.Z. Liu, Y.Q. Cheng, J. Wen, P.L. Lee, W.K. Luo, S.D. Shastri, E. Ma, Polyamorphism in a metallic glass. Nat. Mater. **6**, 192–197 (2007). https://doi.org/10.1038/nmat1839
75. M. Ghidelli, A. Orekhov, A.L. Bassi, G. Terraneo, P. Djemia, G. Abadias, M. Nord, A. Béché, N. Gauquelin, J. Verbeeck, J.-P. Raskin, D. Schryvers, T. Pardoen, H. Idrissi, Novel class of nanostructured metallic glass films with superior and tunable mechanical properties. Acta Mater. **213**, 116955 (2021). https://doi.org/10.1016/j.actamat.2021.116955